PCCP

PAPER

View Article Online
View Journal | View Issue

Cite this: *Phys. Chem. Chem. Phys.*, 2020, **22**, 11984

Influence of alkaline-earth metal substitution on structure, electrical conductivity and oxygen transport properties of perovskite-type oxides $La_{0.6}A_{0.4}FeO_{3-\delta}$ (A = Ca, Sr and Ba)†

Jia Song, [a] De Ning[b] and Henny J. M. Bouwmeester *[a]

Received 15th January 2020,
Accepted 6th May 2020

DOI: 10.1039/d0cp00247j

rsc.li/pccp

Structural evolution, electrical conductivity, oxygen nonstoichiometry and oxygen transport properties of perovskite-type oxides $La_{0.6}A_{0.4}FeO_{3-\delta}$ (A = Ca, Sr, and Ba) were investigated. $La_{0.6}Ca_{0.4}FeO_{3-\delta}$ (LCF64) and $La_{0.6}Sr_{0.4}FeO_{3-\delta}$ (LSF64) show a phase transformation in air at elevated temperature, *i.e.*, from orthorhombic (*Pnma*) to rhombohedral ($R\bar{3}c$) and from rhombohedral to cubic ($Pm\bar{3}m$), respectively, while $La_{0.6}Ba_{0.4}FeO_{3-\delta}$ (LBF64) remains cubic over the entire temperature range from room temperature to 1000 °C. The different phase behaviour of the solids is interpreted to reflect the decreased tendency for octahedral tilting with increasing alkaline-earth-metal dopant ion radius. The electrical conductivity of LSF64 is 191 S cm^{-1} in air at 800 °C, decreasing to a value of 114 S cm^{-1} at a pO_2 of 0.01 atm, and found over this pO_2 range roughly twice as high as those of LCF64 and LBF64. Failure to describe the data of electrical conductivity using Holstein's small polaron theory is briefly discussed. Chemical diffusion coefficients and surface exchange coefficients of the materials in the range 650–900 °C were extracted from data of electrical conductivity relaxation. Data of oxygen nonstoichiometry was used to calculate the vacancy diffusion coefficients from the measured chemical diffusion coefficients. The calculated migration enthalpies are found to decrease in the order LCF64 (1.08 ± 0.04 eV) > LSF64 (0.95 ± 0.01 eV) > LBF64 (0.81 ± 0.01 eV). The estimated ionic conductivities of the materials, at 900 °C, are within a factor of 1.4.

Introduction

In the global effort to develop efficient alternatives to fossil fuel combustion for energy generation, solid oxide fuel cells (SOFCs) have attracted extensive attention due to their high energy conversion efficiency, wide fuel options, and low pollutant emission.[1] To overcome performance degradation, researchers endeavour to lower the operating temperature. A key challenge thereby is to improve the performance of the cathode.

Mixed ionic–electronic conductivity is claimed essential to the cathode to achieve high performance.[2] To date, mixed conducting acceptor-doped ABO_3-type perovskite-structured oxides like $La_{0.6}Sr_{0.4}Co_{0.2}Fe_{0.8}O_{3-\delta}$ (LSCF6428),[3,4] $La_{1-x}Sr_xFeO_{3-\delta}$[5–7] and $La_{0.6}Sr_{0.4}CoO_{3-\delta}$ (LSC64)[8] are being investigated intensively for use as cathode in intermediate-temperature SOFCs (IT-SOFCs).[9–11] Oxygen migration in these materials occurs by the vacancy mechanism. A-site substitution by divalent alkaline-earth metal ions thereby serves to create oxygen vacancies and, thus, to enhance ionic conductivity.[4,12,13]

A few studies have attempted to address the influence of alkaline-earth metal substitution on oxygen transport of (Co,Fe)-based perovskite-type oxides. Teraoka *et al.*[14] first reported the oxygen permeation rate of $La_{0.6}A_{0.4}Co_{0.8}Fe_{0.2}O_{3-\delta}$ to decrease in the order of the dopant Ba > Ca > Sr at 900 °C. A similar sequence was confirmed in a subsequent study on $La_{0.4}A_{0.6}Co_{0.2}Fe_{0.8}O_{3-\delta}$ by Tsai *et al.*[15] Stevenson *et al.*,[16] on the other hand, found the oxygen flux for this series to decrease in the order Sr > Ba > Ca, similar to that observed for $La_{0.2}A_{0.8}Co_{0.2}Fe_{0.8}O_{3-\delta}$.[17] Oxygen fluxes and ionic conductivities of several mixed-conducting perovskite oxides reported by different research groups are compiled in Table 1.

As far as thermal and reduction stability is concerned, cobalt-free materials offer better opportunities to develop stable electrodes, irrespective of the relatively high costs of cobalt. Among the alkaline-earth metals, *ab initio* calculations predict that strontium and calcium would have the lowest solution energies in $LaFeO_3$.[18] Bidrawn *et al.*[19] reported the oxygen permeation rate of $La_{0.8}A_{0.2}FeO_{3-\delta}$ between 650 °C and 800 °C to decrease in the

[a] *Electrochemistry Research Group, Membrane Science and Technology, MESA+ Institute for Nanotechnology, University of Twente, P.O. Box 217, 7500 AE, Enschede, The Netherlands. E-mail: h.j.m.bouwmeester@utwente.nl*
[b] *Helmholtz-Zentrum Berlin für Materialien und Energie, Hahn-Meitner-Platz 1, 14109 Berlin, Germany*

† Electronic supplementary information (ESI) available. See DOI: 10.1039/d0cp00247j

Table 1 Oxygen fluxes and ionic conductivities of $La_{1-x}A_xCo_{1-y}Fe_yO_{3-\delta}$ (A = Ca, Sr, Ba; x = 0.2, 0.4, 0.6, 0.8; y = 0, 0.2, 0.8) reported in the open literature

Materials	Thickness (cm)	j_{O_2} (T (°C)) ($cm^3\ cm^{-2}\ min^{-1}$)	σ_{ion} ($S\ cm^{-1}$)	Ref.
$La_{0.6}Ca_{0.4}Co_{0.8}Fe_{0.2}O_{3-\delta}$	0.2	1.80 (900 °C)	—	14
$La_{0.6}Sr_{0.4}Co_{0.8}Fe_{0.2}O_{3-\delta}$	0.2	0.62 (900 °C)	—	
$La_{0.6}Ba_{0.4}Co_{0.8}Fe_{0.2}O_{3-\delta}$	0.2	2.11 (900 °C)	—	
$La_{0.4}Ca_{0.6}Co_{0.2}Fe_{0.8}O_{3-\delta}$	0.055	0.19 (900 °C)	—	15
$La_{0.4}Sr_{0.6}Co_{0.2}Fe_{0.8}O_{3-\delta}$	0.055	0.11 (900 °C)	—	
$La_{0.4}Ba_{0.6}Co_{0.2}Fe_{0.8}O_{3-\delta}$	0.055	0.72 (900 °C)	—	
$La_{0.4}Ca_{0.6}Co_{0.2}Fe_{0.8}O_{3-\delta}$	0.2	0.07 (900 °C)	0.03 (900 °C)	16
$La_{0.4}Sr_{0.6}Co_{0.2}Fe_{0.8}O_{3-\delta}$	0.2	0.55 (900 °C)	0.40 (900 °C)	
$La_{0.4}Ba_{0.6}Co_{0.2}Fe_{0.8}O_{3-\delta}$	0.2	0.45 (900 °C)	0.33 (900 °C)	
$La_{0.2}Ca_{0.8}Co_{0.2}Fe_{0.8}O_{3-\delta}$	0.1	0.12 (950 °C)	—	17
$La_{0.2}Sr_{0.8}Co_{0.2}Fe_{0.8}O_{3-\delta}$	0.2	0.81 (950 °C)	—	
$La_{0.2}Ba_{0.8}Co_{0.2}Fe_{0.8}O_{3-\delta}$	0.2	0.40 (950 °C)	—	
$La_{0.8}Ca_{0.2}FeO_{3-\delta}$	0.3	—	0.0008 (800 °C)	19
$La_{0.8}Sr_{0.2}FeO_{3-\delta}$	0.3	—	0.0045 (800 °C)	
$La_{0.8}Ba_{0.2}FeO_{3-\delta}$	0.3	—	0.0019 (800 °C)	

order Sr > Ba > Ca. To the best of our knowledge, no other studies have been conducted on the role of the dopant on oxygen transport of $La_{1-x}A_xFeO_{3-\delta}$. In this study, the influence of the nature of the alkaline-earth metal dopant (Ca, Sr, and Ba) on electrical conductivity and oxygen transport of $La_{0.6}A_{0.4}FeO_{3-\delta}$ was investigated by means of electrical conductivity relaxation (ECR). To enable comparison materials with the same alkaline-earth metal dopant concentration were prepared. A dopant concentration of 40 mol% was chosen as Price *et al.*[20] reported formation of secondary phases in samples $La_{1-x}Ca_xFeO_{3-\delta}$ with higher calcium substitution levels. Crystal structure and oxygen non-stoichiometry of the materials were investigated by high-temperature X-ray diffraction (HT-XRD) and thermogravimetric analysis (TGA).

Experimental

Sample preparation

Powders of $La_{0.60}A_{0.40}FeO_{3-\delta}$ (A = Ca, Sr, and Ba) were prepared *via* a modified Pechini method as described elsewhere.[21] Stoichiometric amounts of $La(NO_3)_3{\cdot}6H_2O$ (Alfa Aesar, 99.9%), $Ca(NO_3)_2{\cdot}4H_2O$ (Sigma-Aldrich, 99%), $Sr(NO_3)_2$ (Sigma-Aldrich, ≥99%), $Ba(NO_3)_2$ (Sigma-Aldrich, ≥99%), and $Fe(NO_3)_3{\cdot}9H_2O$ (Sigma-Aldrich, ≥98%) were dissolved in water followed by the addition of $C_{10}H_{16}N_2O_8$ (EDTA, Sigma-Aldrich, >99%) and $C_6H_8O_7$ (citric acid, Alfa Aesar, >99.5%) as chelating agents. The pH of the solution was adjusted to 7 using concentrated NH_4OH (Sigma-Aldrich, 30% w/v). After evaporation of the water, the foam-like gel reached self-ignition at around 350 °C. The obtained raw ashes were calcined at 900 °C for 5 h, using heating/cooling rates of 5 °C min^{-1}. Powders were pelletized by uniaxial pressing at 25 MPa followed by isostatic pressing at 400 MPa for 2 min. Subsequently, the pellets were sintered at 1100–1150 °C for 5 h in air with a heating/cooling rate of 2 °C min^{-1}. The relative density of the pellets was above 94% of their theoretical value as measured by Archimedes' method.

X-ray diffraction

Calcined powders were studied by room-temperature X-ray diffraction (XRD, D2 PHASER, Bruker) with Cu-Kα_1 radiation (λ = 1.54060 Å). Data were collected in the step-scan mode over the 2θ range 20–90° with a step size of 0.01° and a counting time of 8 s. The thermal evolution of the structure was investigated using high-temperature X-ray diffraction (HT-XRD, D8 Advance, Bruker) in air in the range 600–1000 °C with 25 °C intervals. The sample was heated to the desired temperature with a heating rate of 25 °C min^{-1}, followed by a dwell of 5 min to ensure equilibration. XRD patterns were recorded in the 2θ range of 20–90° with a step size of 0.015° and a counting time of 1.3 s. The FullProf software package was used for Rietveld refinements of the patterns.[22]

Oxygen nonstoichiometry

The oxygen nonstoichiometry of $La_{0.60}A_{0.40}FeO_{3-\delta}$ (A = Ca, Sr, and Ba) was determined by thermogravimetric analysis (TGA, Netsch STA F3 Jupiter). Data were collected upon cooling from 900 °C to 650 °C, with intervals of 25 °C and a dwell time of 60 min at each temperature before the start of the measurements. The measurements were conducted in oxygen–nitrogen mixtures containing 4.5%, 10%, 21%, 42% or 90% of O_2, which values correspond to those of the gas streams used in the electrical conductivity relaxation experiments (see below). Prior to data collection, the powder was heated under 4.5% O_2 to 900 °C, with a heating rate of 20 °C min^{-1} and a dwell time of at least 2.5 h, to remove impurities like adsorbed water and CO_2. The dwell time after a pO_2 step at each measurement temperature was 10 min. Following prior studies on $La_{1-x}Sr_xFeO_{3-\delta}$ ($0 \le x \le 0.6$),[23] all compositions were considered to be stochiometric ($\delta = 0$) at a pO_2 of 0.21 atm below 150 °C.

Electrical conductivity relaxation

Samples for ECR measurements were prepared by grinding and cutting the obtained dense pellets to planar sheet-shaped samples with approximate dimensions 12 × 5 × 0.5 mm^3. The sample surface was polished using diamond polishing discs (JZ Primo, Xinhui China) down to 0.5 μm. A four-probe DC method was used to collect data of electrical conductivity. Two gold wires (Alfa Aesar, 99.999%, ∅ = 0.25 mm) were wrapped around both ends of the sample for current supply. Two additional gold wires were wrapped 1 mm remote from the current electrodes to act as voltage probes. To ensure good contact between the gold wires and the sample, sulphur-free gold paste (home-made) was applied on the sample surface directly underneath the gold wires. Finally, the sample was annealed at 950 °C in air for 1 h to sinter the gold paste and thermally cure the polished sample surface.

The sample was mounted on a holder and placed in an alumina sample containment chamber (or reactor). Two gas streams, each of which with a flow rate of 280 ml min^{-1} and with a different pO_2, were created by mixing dried oxygen and nitrogen in the desired ratios using Brooks GF040 mass flow controllers. A pneumatically operated four-way valve was used

to instantaneously switch between both gas streams so that one of them was fed through the reactor. Data of the transient electrical conductivity was collected following oxidation and reduction step changes in pO_2 between 0.10 and 0.21 atm. Measurements were conducted following stepwise cooling from 900 °C to 650 °C with intervals of 25 °C, heating and cooling rates of 10 °C min^{-1} and a dwell time of 60 min at each temperature before data acquisition.

The transient conductivity after each pO_2 step change was normalized according to eqn (1) and fitted to eqn (2)–(4) to obtain the chemical diffusion coefficient D_{chem} and the surface exchange coefficient k_{chem}.

$$g(t) = \frac{\sigma(t) - \sigma_0}{\sigma_\infty - \sigma_0} \tag{1}$$

$$g(t) = 1 - \prod_{i=y,z} \sum_{m=1}^{\infty} \frac{2L_i^2}{\beta_{m,i}^2\left(\beta_{m,i}^2 + L_i^2 + L_i\right)} \frac{\tau_{m,i}}{\tau_{m,i} - \tau_{\mathrm{f}}} \times \left(e^{-\frac{t}{\tau_{m,i}}} - \frac{\tau_{\mathrm{f}}}{\tau_{m,i}}\left(e^{-\frac{t}{\tau_{\mathrm{f}}}}\right)\right) \tag{2}$$

$$\tau_{m,i} = \frac{b_i^2}{D_{\mathrm{chem}}\beta_{m,i}^2} \tag{3}$$

$$L_i = \frac{b_i}{L_{\mathrm{c}}} = \beta_{m,i} \tan \beta_{m,i} \tag{4}$$

In these equations, $g(t)$ is the normalized conductivity, σ_0 and σ_∞ are the conductivities $\sigma(t)$ at time $t = 0$ and $t = \infty$, respectively, τ_{f} is the flush time, $2b_i$ is the sample dimension along coordinate i, whilst $\beta_{m,i}$ are the non-zero roots of eqn (4). $L_{\mathrm{c}} = D_{\mathrm{chem}}/k_{\mathrm{chem}}$ is the critical thickness below which oxygen surface exchange prevails over bulk oxygen diffusion in determining the rate of re-equilibration after a pO_2 step change. The flush time τ_{f} was calculated from

$$\tau_{\mathrm{f}} = \frac{V_{\mathrm{r}}}{\theta_{\mathrm{v}}} \frac{T_{\mathrm{STP}}}{T_{\mathrm{r}}} \tag{5}$$

which equation assumes perfect mixing of the gas in the sample containment chamber. In eqn (5), V_{r} is the corresponding volume, θ_{v} the gas flow rate through the chamber, T_{r} the temperature inside the chamber, and T_{STP} the temperature at standard conditions. The small chamber volume (2.58 cm^3) and the high gas flow rate (280 ml min^{-1}) used ensured a flush time between 0.13 s at 900 °C and 0.16 s at 650 °C. Curve fitting of the normalized transient conductivity was performed using a non-linear least-squares program based on the Levenberg–Marquardt algorithm. More detailed descriptions of the ECR technique and the model used for data fitting are given elsewhere.[24,25]

Results and discussion

Crystal structure and phase transitions

Fig. 1 shows the room temperature XRD patterns of LCF64, LSF64 and LBF64 recorded in air. The corresponding structural parameters and reliability factors from Rietveld refinements are

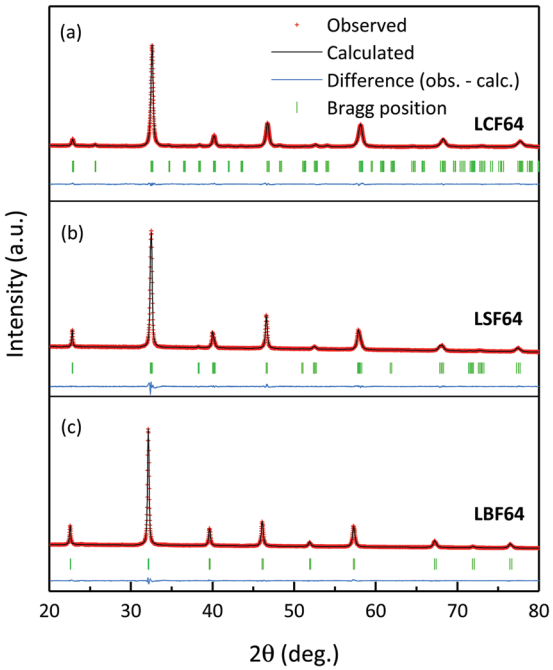

Fig. 1 Measured (red symbols) and calculated (black line) of room temperature XRD powder patterns of LCF64, LSF64 and LBF64. Bragg peaks and the residual plots are given under the patterns.

Table 2 Space group, lattice parameters and reliability factors obtained from the Rietveld refinements of room temperature XRD diffractograms of LCF64, LSF64 and LBF64. The lattice parameters for the rhombohedral ($R\bar{3}c$) structure of LSF64 are listed in hexagonal settings. The numbers in parentheses denote standard deviations in units of the least significant digits

	LCF64	LSF64	LBF64
Space group	*Pnma*	$R\bar{3}c$	$Pm\bar{3}m$
a/Å	5.5138(1)	5.5226(1)	3.93652(2)
b/Å	7.7574(1)	5.5226(1)	3.93652(2)
c/Å	5.4896(1)	13.4462(3)	3.93652(2)
V/Å^3	234.8064(2)	355.1558(2)	61.0014(1)
R_{wp}/%	5.49	7.55	6.03
R_{Bragg}/%	1.79	1.01	1.042
χ^2	4.78	2.55	3.545

listed in Table 2. No impurity peaks are found in the patterns, suggesting that all three compositions are single phase. The pattern obtained for LCF64 could be fitted with an orthorhombic structure (space group *Pnma*) with cell parameters a = 5.4962(2) Å, b = 7.7658(2) Å and c = 5.5018(2) Å, which is in excellent agreement with a = 5.4941 Å, b = 7.7736 Å and c = 5.5083 Å reported by Hung *et al.*[26] LSF64 adopts a rhombohedral structure (space group $R\bar{3}c$) with cell parameters a = 5.5228(1) Å and c = 13.4471(3) Å (hexagonal representation), in good agreement with a = 5.5272(2) Å and c = 13.4408(4) Å reported by Yang *et al.*[27] LBF64 appears to be cubic (space group $Pm\bar{3}m$) with a = 3.93652(2) Å, matching precisely the value a = 3.93652(9) Å found for $La_{0.5}Ba_{0.5}FeO_{3-\delta}$ reported by Ecija *et al.*[28]

HT-XRD patterns of LCF64, LSF64 and LBF64 are shown in Fig. S1 (ESI†). Pseudo-cubic lattice parameters obtained from

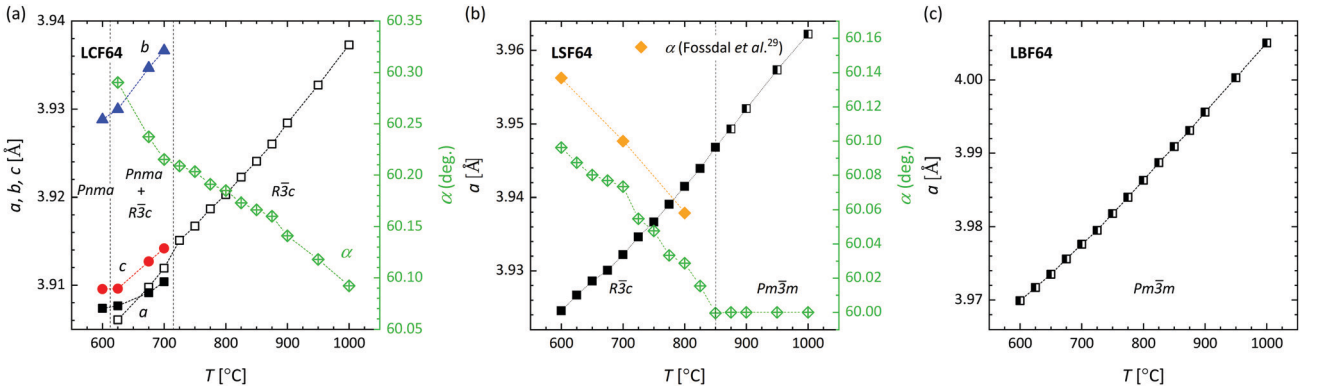

Fig. 2 Lattice parameters for (a) LCF64, (b) LSF64, (c) LBF64 as a function of temperature from Rietveld refinements of HT-XRD patterns recorded in air. Pseudo-cubic cell parameters are given for the orthorhombic (*Pnma*) structures, calculated using $a = a_{ortho}/\sqrt{2}$, $b = b_{ortho}/2$ and $c = c_{ortho}/\sqrt{2}$. For the cubic ($Pm\bar{3}m$) and rhombohedral ($R\bar{3}c$) structures $a = b = c$.

Rietveld refinements of these are shown in Fig. 2. Price *et al.*[20] verified the occurrence of a phase transition sequence in LCF64, *i.e.*, from orthorhombic (space group *Pnma*) to rhombohedral (space group $R\bar{3}c$) at 602 °C to cubic (space group $Pm\bar{3}m$) at about 1100 °C, on the basis of data of differential scanning calorimetry (DSC) and HT-XRD. Our study confirms that LCF64 remains orthorhombic until ~600 °C, consistent with the results obtained by Price *et al.*[20] However, our refinements yield a mixture of orthorhombic and rhombohedral phases above ~625 °C, *i.e.*, from 3.89% rhombohedral at 625 °C to 15.79% at 700 °C, transforming into a pure rhombohedral phase above 725 °C. The rhombohedral angle decreases from 60.29° at 625 °C to 60.09° at 1000 °C, suggesting that at a slightly higher temperature the cubic phase is formed. Fig. 2b shows the occurrence of a rhombohedral-to-cubic phase transition in LSF64 at around 850 °C, which is in agreement with previous results obtained by Fossdal *et al.*[29] LBF64 adopts a cubic structure (space group $Pm\bar{3}m$) throughout the measured temperature range, as shown in Fig. 2c. The temperature dependences of the Fe–O–Fe angles and Fe–O bond lengths obtained from the Rietveld refinements are plotted in Fig. S2 (ESI†).

The crystal symmetry of the room-temperature structure is found to decrease in the order LBF64, LSF64 and LCF64, *i.e.*, from cubic to rhombohedral to orthorhombic, respectively, following the decrease in the magnitude of the radii of the alkaline-earth-metal dopant ions: Ba^{2+} (XII) = 1.61 Å > Sr^{2+} (XII) = 1.44 Å > Ca^{2+} (XII) = 1.34 Å, where the number between brackets designates the coordination number. Ionic radii were taken from Shannon.[30] The observed lowering in symmetry is believed to result from cooperative tilting of BO_6 octahedra, which is the most commonly observed distortion in perovskite structures. The tendency for distortion of the ABO_3 perovskite structure is generally rationalized by the Goldschmidt tolerance factor $t = (r_A + r_O)/\sqrt{2}(r_B + r_O)$,[31] where r_A, r_B and r_O are the ionic radii of the involved ions. The ideal cubic structure is formed for $t = 1$, when the A and O^{2-} ions are matching in size to form cubic close-packed layers, while the B cations fit into the interstices formed by the O^{2-} ions to give an array of corner-shared BO_6 octahedra. For $t < 1$, the BO_6 octahedra cooperatively tilt to accommodate the mismatch, thereby forming less symmetric rhombohedral or orthorhombic structures.[32,33] The orthorhombic *Pnma* structure, in Glazer's notation[34] denoted by $a^-a^-c^+$, as adopted by LCF64 is one of the most common perovskite structures with a three-tilt system.[35,36] Upon decreasing the size of the earth-alkaline cation, the out-of-phase rotation (−) along the [001] direction of the pseudo-cubic cell changes to an in-phase rotation (−) for LSF64, expressed in Glazer's notation by $a^-a^-c^-$ (space group $R\bar{3}c$), and to the no-tilt system $a^0a^0a^0$ (space group $Pm\bar{3}m$) for LBF64. Note from Fig. 2a and b that similar structural changes are induced in LCF64 and LSF64 upon increasing temperature.

Oxygen stoichiometry

The oxygen stoichiometry $(3 - \delta)$ in LCF64, LSF64 and LBF64 as a function of oxygen partial pressure and temperature was investigated by thermogravimetry. A typical measurement scheme is shown in Fig. S3 (ESI†). Corresponding data obtained at different temperatures is shown in Fig. 3. For completeness, plots of $\log(\delta)$ *vs.* $\log(pO_2)$ at different temperatures for each of the compositions are given in Fig. S4 (ESI†). As can be inferred from the data of Fig. 3, the oxygen content in the experimental range of temperature and oxygen partial pressure tends to increase in the order LBF64 < LSF64 < LCF64. Good agreement was obtained between the results of this study for LSF64 and corresponding data measured at 800 °C and 900 °C by Kuhn *et al.*[37] as demonstrated in Fig. S5 (ESI†). To the best of our knowledge, no data of oxygen stoichiometry has been reported for LCF64 and LBF64. Kharton *et al.*[38] measured the pO_2 dependence of the oxygen contents of $La_{0.5}Sr_{0.5}FeO_{3-\delta}$ and $La_{0.5}Ba_{0.5}FeO_{3-\delta}$, at 950 °C, yielding trends similar to those found in Fig. 3.

Electrical conductivity

Fig. 4a and Fig. S6a (ESI†) show that over the entire experimental range of temperature and oxygen partial pressure, the electrical conductivity of LSF64 is roughly twice as high as those of LBF64 and LCF64. At 800 °C, the conductivity of LSF64 in air is 191 S cm^{-1}, to be compared with values of 91 S cm^{-1} and 93 S cm^{-1} measured under these conditions for LCF64 and LBF64, respectively. Excellent agreement is found between the results for LSF64 from this

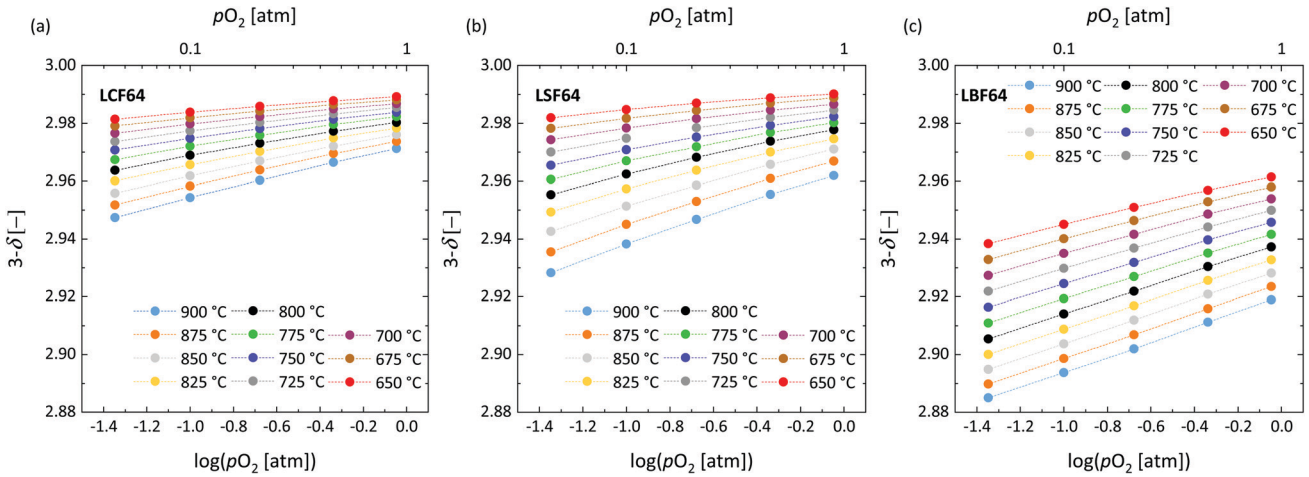

Fig. 3 Oxygen stoichiometry of (a) LCF64, (b) LSF64 and (c) LBF64 as a function of $\log(pO_2)$ at different temperatures. Dashed lines are drawn to guide the eye.

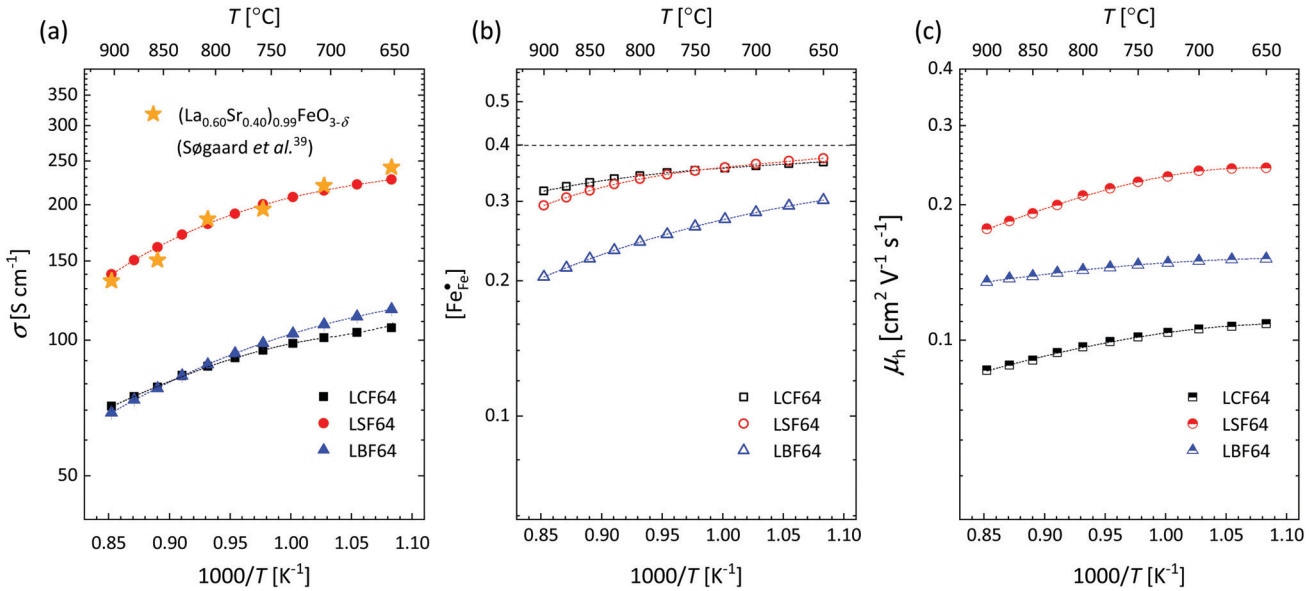

Fig. 4 Arrhenius plots of the (a) electrical conductivity, (b) defect concentration $[Fe^{\bullet}_{Fe}]$ and (c) mobility of electron–holes, at pO_2 = 0.21 atm, for LCF64, LSF64 and LBF64. The dashed lines through the data points are drawn to guide the eye. The horizontal line in Fig. 4b represents the $[Fe^{\bullet}_{Fe}]$ concentration when electronic compensation is predominant, noting that all three materials have the same concentration of the alkaline-earth dopant (*cf.* eqn (7)).

study and data reported by Søgaard *et al.*,[39] as demonstrated in Fig. 4a.

The electrical conductivity in $La_{1-x}A_xFeO_{3-\delta}$ (A = Ca, Sr, Ba) and related perovskite oxides is commonly interpreted on the basis of hopping of small polarons.[26,40–42] Under oxidizing atmospheres, the conductivity can be expressed as,[26,43]

$$\sigma = \frac{p}{V_m} e \mu_h \quad (6)$$

where p and μ_h are the concentration (mole fraction) and mobility of electron holes, respectively, V_m is the unit cell volume, and e is the electronic charge. Both parameters p and μ_p are considered to be thermally activated. The partial substitution of lanthanum in $La_{1-x}A_xFeO_{3-\delta}$ (A = Ca, Sr, Ba) by divalent alkaline-earth ions is charge compensated by the formation of electron holes and/or oxygen vacancies, the limiting cases being referred to as electronic and ionic compensation, respectively. Assuming oxygen vacancies to be doubly ionized, the reduced charge neutrality condition can be written as, in Kröger–Vink notation,[44]

$$[A'_{La}] = 2[V^{\bullet\bullet}_O] + [Fe^{\bullet}_{Fe}] \quad (7)$$

where $[Fe^{\bullet}_{Fe}] \equiv p$ represents the concentration of p-type charge carriers. Eqn (7) lacks n-type charge carriers, Fe'_{Fe}, arising as a result of the charge disproportionation reaction,

$$Fe^{\times}_{Fe} \rightleftharpoons Fe'_{Fe} + Fe^{\bullet}_{Fe} \quad (8)$$

and which become dominant under reducing atmospheres. In the case of structural A- and B-site deficiency, also vacancies V'''_{La} and

V'''_{Fe} need to be taken into account. Using eqn (7) and data of oxygen stoichiometry (Fig. 3), the concentration of $Fe^{\bullet}_{Fe}$ in phases LCF64, LSF64 and LBF64 may be calculated. Corresponding data are shown in Fig. 4b and Fig. S6b (ESI†), from which figures it can be inferred that under the conditions covered by the experiments electronic compensation dominates over ionic compensation. The lowest electron–hole concentration is found in LBF64, indicating that in this material the relative contribution of the ionic compensation mechanism is higher than those in LCF64 and LSF64. In all three phases, the concentration $[Fe^{\bullet}_{Fe}]$ is found to decrease and, hence, ionic compensation appears to become more dominant, with increasing temperature and decreasing oxygen partial pressure.

Electrical mobilities of the electron holes calculated using eqn (6) plotted as a function of inverse temperature and $\log(pO_2)$ are presented in Fig. 4c and Fig. S6c (ESI†), respectively. Below, we have analysed the inverse temperature dependence of the electron–hole mobility in terms of Holstein's generalized small polaron model (in which the initial and final states are treated on equal footing), considering both adiabatic and non-adiabatic hopping.[46–48] In the adiabatic case,[46] the charge carrier is able to hop to an adjacent vacant site, once an energy coincidence occurs. The corresponding mobility of electron holes is given by

$$\mu_h = (1 - [Fe^{\bullet}_{Fe}])\frac{3}{2}\frac{ea^2\nu_0}{k_B T}\exp\left(-\frac{\frac{1}{2}W_p - J}{k_B T}\right) \quad (9)$$

where a is the hopping distance, ν_0 is the frequency of optical phonons, W_p is the polaron binding energy, J is the kinetic energy of the polaron, and k_B is the Boltzmann constant. The factor of 3/2 takes into account the fact that the polaron moves in a three-dimensional lattice.[46] The factor of $(1 - [Fe^{\bullet}_{Fe}])$ takes into account the site-blocking effect, the probability that the adjacent site to which the polaron hops may already be occupied.[48] In the non-adiabatic case,[45] the polaron misses coincidence events as it moves too slowly, lowering the net hopping rate. In this case, the mobility of electron holes is given by

$$\mu_h = (1 - [Fe^{\bullet}_{Fe}])\frac{3}{2}\frac{ea^2}{k_B T}\frac{\pi J^2}{h}\left(\frac{2\pi}{W_p k_B T}\right)^{1/2}\exp\left(-\frac{\frac{1}{2}W_p}{k_B T}\right) \quad (10)$$

where h is the Planck constant. In the adiabatic regime, the plot of $\ln\{\mu_h T/(1 - [Fe^{\bullet}_{Fe}])\}$ *vs.* $1000/T$ should give a straight line with activation energy $E_a = \frac{1}{2}W_p - J$; in the non-adiabatic regime, the plot of $\ln\{\mu_h T^{3/2}/(1 - [Fe^{\bullet}_{Fe}])\}$ *vs.* $1000/T$ should give a straight line with activation energy $E_a = \frac{1}{2}W_p$.

Corresponding plots are shown in Fig. 5. The plots obtained for LCF64 and LSF64 exhibit a double slope behaviour. At lower temperatures the curves for both materials can be interpreted in a way as characteristic for small polaron conduction (*i.e.*, small polarons have a thermally activated mobility), but at higher temperatures the curves show a negative slope. For LBF64, the apparent activation energy of the mobility is estimated at a value of 0.039 ± 0.002 eV in the non-adiabatic case, while it tends to nearly zero in the adiabatic case. Our results are consistent with those obtained in a study by Patrakeev *et al.*[49] who found an activation energy for the carrier mobility in $La_{1-x}Sr_xFeO_{3-\delta}$ of about 0.4 eV and 0.2 eV for x = 1.0 and x = 0.7, respectively, while tending to values near to zero in the oxides with $x \leq 0.5$. The low activation energies that may be inferred from the data in Fig. 6a and b may be compared with the approximate values 0.04–0.14 eV derived from $\ln\{\sigma T\}$ *versus* $1000/T$ plots for $La_{0.8}Sr_{0.2}Co_{1-y}Fe_yO_{3-\delta}$ ($0 \leq y \leq 1$).[50] It is obvious from the above analysis that other factors need to be considered to account for the observations.

Inspection of the data in Fig. 4 and 5 suggests that the electrical mobility is correlated with the electron hole concentration in phases LCF64, LSF64 and LBF64. The observed trend

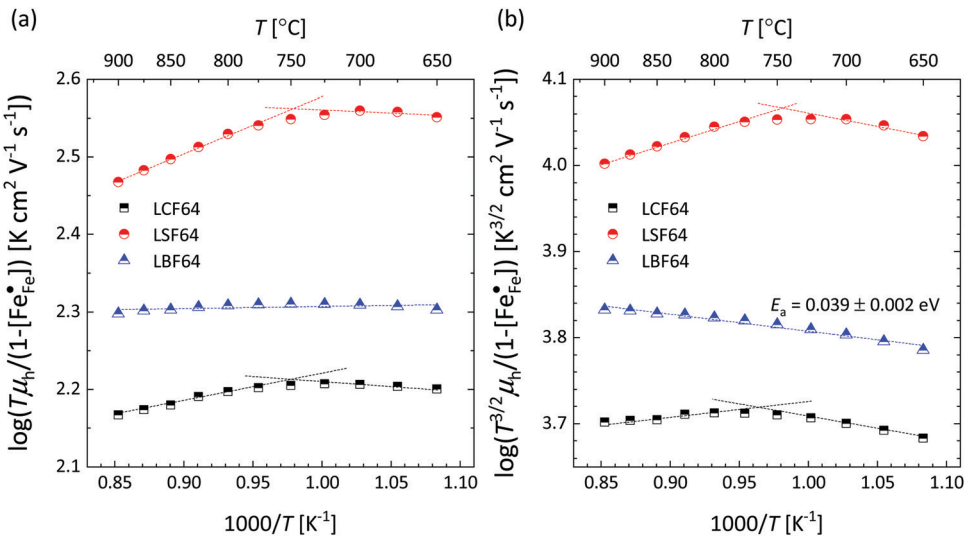

Fig. 5 Plots of (a) $\ln\{\mu_h T/(1 - [Fe^{\bullet}_{Fe}])\}$ *vs.* $1000/T$ (adiabatic case) and (b) $\ln\{\mu_h T^{3/2}/(1 - [Fe^{\bullet}_{Fe}])\}$ *vs.* $1000/T$ (non-adiabatic case), at pO_2 = 0.21 atm. The dotted lines are drawn to guide the eye.

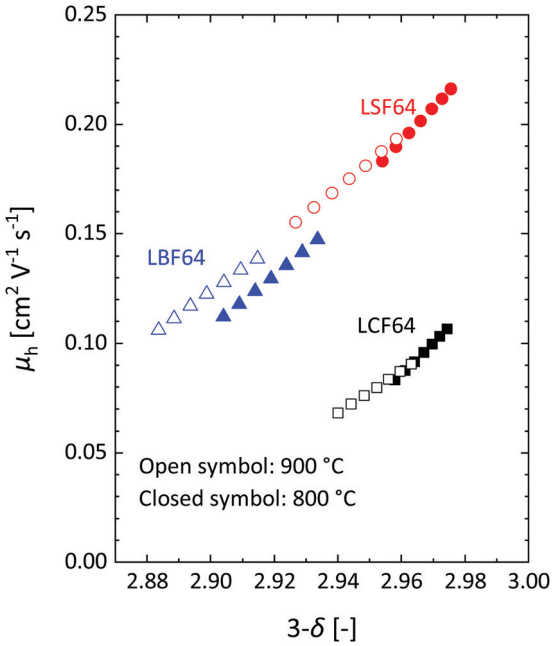

Fig. 6 Mobility of electron–holes, at 800 °C and 900 °C, as a function of oxygen content for LCF64, LSF64 and LBF64.

deduced is that the electrical mobility is suppressed with decreasing the electron hole concentration, $[Fe_{Fe}^{\bullet}]$, which is contrary to what is expected from the site-blocking term, $(1 - [Fe_{Fe}^{\bullet}])$, in eqn (9) and (10). In view of eqn (7), the electron hole concentration on its turn is correlated with the concentration of oxygen vacancies. Fig. 6 shows that the hopping mobility decreases with increasing the oxygen nonstoichiometry of phases LCF64, LSF64 and LBF64. Similar observations have been reported for $La_{1-x}Sr_xFeO_{3-\delta}$ ($0.1 \leq x \leq 1$).[49] Noting that the direct overlap between neighbouring Fe 3d orbitals in the $La_{0.6}A_{0.4}FeO_{3-\delta}$ (A = Ca, Sr, and Ba) perovskite structure is negligible, the polaron hopping between two adjacent Fe cations is brought about by the overlapping O 2p orbitals of the bridging oxygen ion, which is known as the Zener double-exchange mechanism.[51] Disruption of the Fe^{4+}–O–Fe^{3+} migration pathways due to the presence of oxygen vacancies thus may affect the hopping mobility. The probability that an oxygen vacancy blocks the migration pathway scales with $(1 - \delta/3)$. The corresponding values for this parameter for each of the materials under the given experimental conditions are, however, too close to unity to have a significant impact on the effective hopping mobility. Electrostatic interactions between the electron holes and oxygen vacancies or formation of delocalized states may further affect the hopping mobility. X-ray absorption spectroscopy and density functional theory studies indicate that the electron holes in $La_{1-x}Sr_xFeO_{3-\delta}$ and $La_{1-x}Ca_xFeO_{3-\delta}$ have mixed Fe 3d and O 2p band character and, hence, are delocalized at least to some extent.[51–58] This would comply with the observed low-to-zero activation energies of the carrier mobility in phases LCF64, LSF64 and LBF64 (*cf.* Fig. 5). This argument is, however, in contrast with results from angle-resolved photo emission spectroscopy, suggesting a strong localisation of the electron holes in $La_{0.6}Sr_{0.4}FeO_{3-\delta}$.[59] Clearly, more research is warranted to clarify the nature of the charge carriers in $La_{1-x}A_xFeO_{3-\delta}$ (A = Ca, Sr, Ba).

Electrical conductivity relaxation

Chemical diffusion and surface exchange coefficients. In this study, the ECR method was used for evaluation of the oxygen transport properties of LCF64, LSF64 and LBF64. Typical fits to the normalized conductivity relaxation curves following oxidation and reduction step changes in pO_2 are shown in Fig. 7. In general, the curves from oxidation and reduction runs may slightly differ due to the pO_2 dependence of oxygen transport. This asymmetry will be influenced by the mean pO_2 and the magnitude of the pO_2 step size. Curve fitting allows simultaneous determination of the chemical diffusion coefficient D_{chem} and the surface exchange coefficient k_{chem} provided that fitting is sensitive to both parameters. If the smallest dimension of the sample is much lower than the ratio D_{chem}/k_{chem}, the fitting will be insensitive to D_{chem}. Conversely, if the sample dimensions are much lower than D_{chem}/k_{chem}, curve fitting will be insensitive to k_{chem}. Accordingly, one may define a Biot number (Bi),

$$\mathrm{Bi} = \frac{l_z}{D_{chem}/k_{chem}} \quad (11)$$

where l_z is the half thickness of the sample. The Biot number compares the relative rates of oxygen diffusion and surface exchange to the relaxation process. If $\mathrm{Bi} \geq 30$, then the relaxation is said to predominantly controlled by diffusion; if $\mathrm{Bi} \leq 0.03$, then the relaxation is said to predominantly controlled by surface exchange.[25] In the intermediate region, $0.03 \leq \mathrm{Bi} \leq 30$, both diffusion and surface exchange determine the relaxation. The bounds are linked to the accuracy of curve fitting, *i.e.*, only in the mixed controlled region both D_{chem} and k_{chem} can be most reliably assessed. A plot of the Biot number against temperature obtained from fitting data of ECR measurements of LCF64, LSF64 and LBF64 is shown in Fig. 8. Note from eqn (11) that the Biot number can only be calculated if both D_{chem} and k_{chem} are

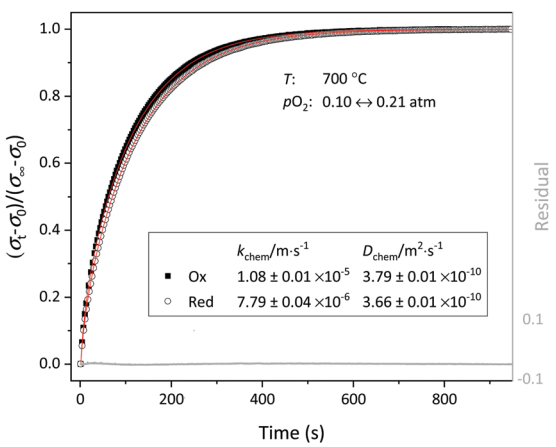

Fig. 7 Normalized conductivity curves obtained for LCF64 following step changes in pO_2 between 0.1 and 0.21 atm at 700 °C. The solid lines show the least-square fits to eqn (2)–(4).

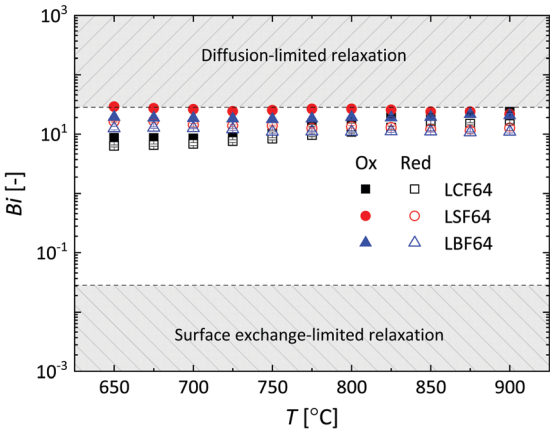

Fig. 8 Temperature dependence of the Biot number (Bi) for LCF64, LSF64 and LBF64. Errors bars are within the symbols.

obtained from curve fitting. D_{chem} and k_{chem} may exhibit different pO_2 dependencies. Therefore, in addition to varying the sample dimension l_z, the measurements can be performed at different oxygen partial pressure to improve the sensitivity of fitting to either D_{chem} or k_{chem}.

Arrhenius plots of D_{chem} and k_{chem} of LCF64, LSF64 and LBF64 derived from the data of ECR measurements are shown in Fig. 9. The corresponding apparent activation energies are listed in Table S2 (ESI†). The D_{chem} values of the different materials show remarkable agreement with an average activation energy close to 93 kJ mol^{-1}. It is further noted from Fig. 9d that the values obtained for LSF64 are in good agreement with previously reported results.[24,39] The values of k_{chem} of the different materials are found to be within similar range above 850 °C. Below this temperature, however, a different activation

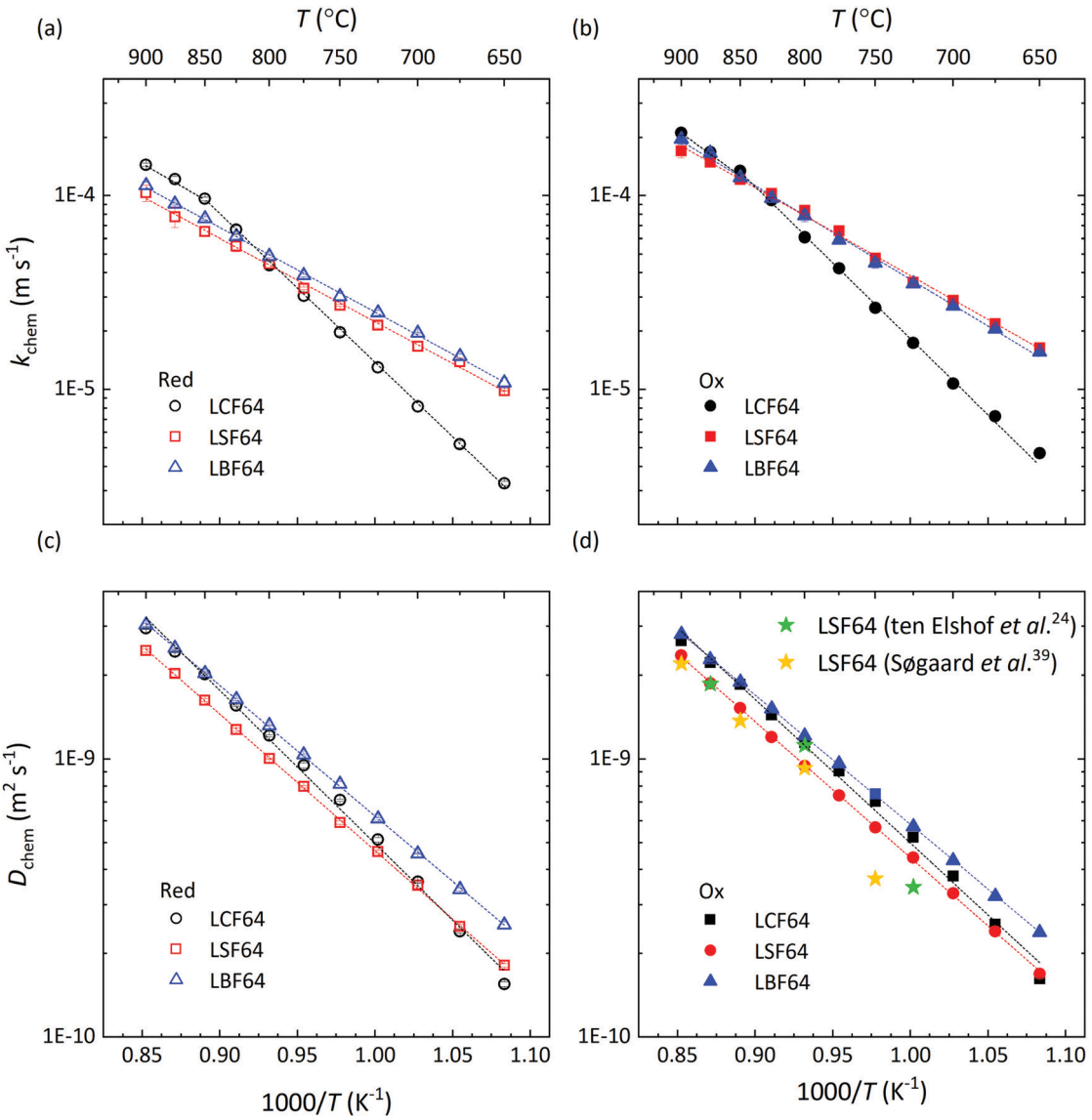

Fig. 9 Arrhenius plots of the (a and b) surface exchange coefficient, k_{chem}, and (c and d) chemical diffusion coefficient, D_{chem}, for LCF64, LSF64 and LBF64. For clarity, data from oxidation (Ox) and reduction (red) runs are given in separate plots. Error bars are within the symbols. The dashed lines are from linear fitting of the data.

energy for k_{chem} is apparent for LCF64 when compared with those found for LSF64 and LBF64 for which behaviour we lack a definite explanation (*cf.* Table S2, ESI†). In general, the surface exchange rate on oxide surfaces may be highly influenced by, *e.g.*, surface enrichment due to segregation, surface impurities and grain size. No attempt was made in this study to relate the elemental surface composition and morphology to the observed surface exchange rates exhibited by the samples.

Oxygen self-diffusion and vacancy-diffusion coefficients. The oxygen self-diffusion coefficients, D_s, and oxygen vacancy-diffusion coefficients, D_v, for phases LCF64, LSF64 and LBF64 were evaluated from the measured values of D_{chem}, using the relationships $D_{chem} = \gamma_O D_s = \gamma_v D_v$,[24] where γ_O and γ_v are the thermodynamic factors, defined as

$$\gamma_O = \frac{1}{2}\cdot\frac{\partial \ln(pO_2)}{\partial \ln(c_O)} = \frac{3-\delta}{2}\cdot\frac{\partial \ln(pO_2)}{\partial(3-\delta)} \quad (12)$$

$$\gamma_v = -\frac{1}{2}\cdot\frac{\partial \ln(pO_2)}{\partial \ln(c_v)} = -\frac{\delta}{2}\cdot\frac{\partial \ln(pO_2)}{\partial \delta} = \frac{\delta}{3-\delta}\gamma_O \quad (13)$$

Herein, c_O and c_v are the concentrations of oxygen ions and vacancies in the lattice. The thermodynamic factors can be derived from corresponding data of the oxygen non-stoichiometry (Fig. 3) and are given for the different phases in Fig. S7 (ESI†). Arrhenius plots of the calculated values of D_s and D_v for the different materials are shown in Fig. 10, while the activation energies extracted from these are listed in Table S3 (ESI†) and Table 3, respectively.

Fig. 10a shows that over the temperature range 650–900 °C almost similar values of D_s are observed for LCF64 and LSF64. Slightly higher values are found for LBF64; the difference is a factor of about 3 at 650 °C, which has reduced to a factor 1.2 at 900 °C due to a slightly lower activation energy of 106 ± 1 kJ mol^{-1} compared with values of 138 ± 2 kJ mol^{-1} and 146 ± 1 kJ mol^{-1} observed for LCF64 and LSF64, respectively. Also shown in in this figure are values of D_s for other compositions in the series for $La_{1-x}Sr_xFeO_{3-\delta}$ from literature,[60,61] demonstrating the expected increase of D_s with increasing the alkaline-earth metal dopant concentration and the consistency with the results from this study. Calculated ionic conductivities of phases LCF64, LSF64, and LBF64, using the Nernst–Einstein equation are given in Fig. 11. As the total concentration of oxygen ions remains virtually constant, the trend in ionic conductivity among the different materials is the same as that observed for D_s (*cf.* Fig. 9a). Fig. 10b shows that the values of D_v of phases LCF64, LSF64 and LBF64 in the experimental temperature range are very similar, which further indicates that the higher ionic conductivities and self-diffusion coefficients observed for LBF64 relative to corresponding values for LCF64 and LSF64 at similar conditions are mainly due to the higher concentration oxygen vacancies in the former material. The observed trend among the ionic conductivities of LCF64, LSF64 and LBF64 differs from that previously reported for $La_{0.8}A_{0.2}FeO_{3-\delta}$

Table 3 Migration enthalpies (ΔH_m) of LCF64, LSF64 and LBF64 extracted from data of ECR experiments, following pO_2 step changes 0.21 → 0.1 atm (Red) and 0.1 → 0.21 atm (Ox)

	Red	Ox
Materials	ΔH_m (eV)	ΔH_m (eV)
LCF64	1.11 ± 0.03	1.05 ± 0.03
LSF64	0.94 ± 0.01	0.96 ± 0.01
LBF64	0.80 ± 0.01	0.82 ± 0.01

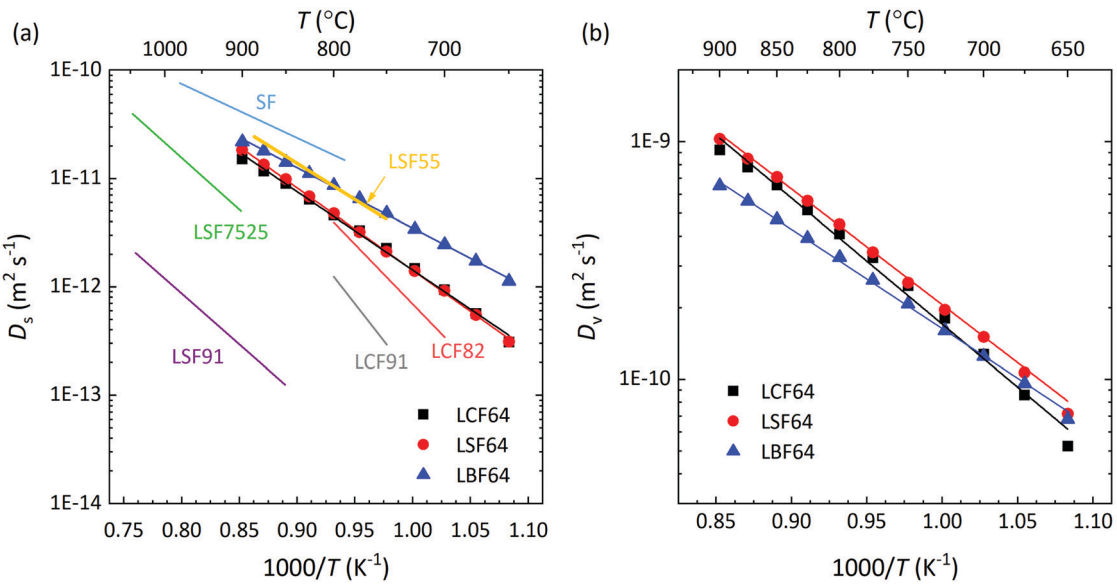

Fig. 10 Arrhenius plots of the (a) self-diffusion coefficient, D_s, and (b) vacancy-diffusion coefficient, D_v, at pO_2 = 0.142 atm, for LCF64, LSF64 and LBF64. The specified pO_2 corresponds to the logarithmic average of the initial and final values of the pO_2 step change during ECR experiments. For clarity, only data of oxidations runs are shown in both figures. Error bars are within the symbols. The drawn lines are from linear fitting of the data. Also shown in (a) are values of D_s for $La_{0.9}Sr_{0.1}FeO_{3-\delta}$ (LSF91) and $La_{0.75}Sr_{0.25}FeO_{3-\delta}$ (LSF7525), at pO_2 = 0.65 atm,[60] calculated from data of isotopic exchange depth profiling (IEDP), and for $La_{0.5}Sr_{0.5}FeO_{3-\delta}$ (LSF55) and $SrFeO_{3-\delta}$ (SF), at pO_2 = 0.05 atm, from data of ECR.[61]

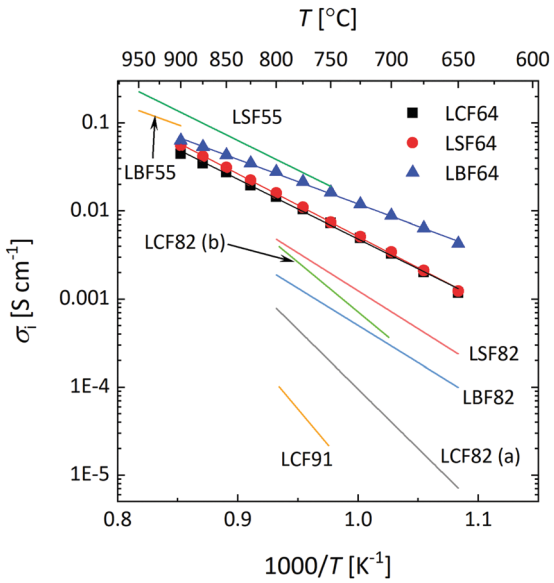

Fig. 11 Arrhenius plots of the ionic conductivity of LCF64, LSF64 and LBF64, at pO_2 = 0.142 atm. The specified pO_2 corresponds to the logarithmic average of the initial and final values of the pO_2 step change during ECR experiments. Lines are drawn to guide the eye. Data taken from literature are shown for comparison: $La_{0.5}Sr_{0.5}FeO_{3-\delta}$ (LSF55),[38] $La_{0.5}Ba_{0.5}FeO_{3-\delta}$ (LBF55),[38] $La_{0.8}Ca_{0.2}FeO_{3-\delta}$ (LCF82 (a)),[19] $La_{0.8}Sr_{0.2}FeO_{3-\delta}$ (LSF82),[19] $La_{0.8}Ba_{0.2}FeO_{3-\delta}$ (LBF82),[19] $La_{0.8}Ca_{0.2}FeO_{3-\delta}$ (LCF82 (b)),[63] $La_{0.9}Ca_{0.1}FeO_{3-\delta}$ (LCF91).[64]

(A = Ca, Sr, Ba) by Bidrawn *et al.*[19] (see Fig. 11). Estimating the ionic conductivity from data of oxygen permeation measurements performed in the range 650–800 °C, these authors showed that $La_{0.8}Sr_{0.2}FeO_{3-\delta}$ (LSF82) exhibits the highest ionic conductivities, followed by $La_{0.8}Ba_{0.2}FeO_{3-\delta}$ (LBF82) and $La_{0.8}Ca_{0.2}FeO_{3-\delta}$ (LCF82). The different trend may – at least at first glance – be due to a different alkaline-earth metal dopant concentration used in the study by Bidrawn *et al.*[19] However, estimates of the ionic conductivity from data of oxygen permeation may be erroneous in case of – and ignoring – partial rate limitations by the surface exchange reactions.[62] There is some evidence for the latter when the comparison of ionic conductivities in Fig. 11 is extended to include data for $La_{0.9}Ca_{0.1}FeO_{3-\delta}$ (LCF91) and $La_{0.8}Ca_{0.2}FeO_{3-\delta}$ (LCF82) as derived from data of ECR experiments by Berger *et al.*[63,64] Clearly, more work is required to resolve the apparent discrepancies between the results of different studies.

The type of alkaline-earth metal ion within the experimental temperature range appears to have little impact on the oxygen vacancy mobility. The calculated average migration enthalpies, however, show a clear trend, decreasing in the order LCF (1.08 ± 0.04 eV) > LSF64 (0.95 ± 0.01 eV) > LBF64 (0.81 ± 0.01 eV) (*cf.* Table 3). Oxygen migration in the perovskite structure is known to occur *via* an energetic saddle point defined as the triangle formed by one B site cation and two A site cations between two adjacent OA_4B_2 octahedra.[65] From a purely ionic point of view, the observed lowering in migration enthalpy in the series is expected from the trend in polarizability, $\alpha_{Ba^{2+}} > \alpha_{Sr^{2+}} > \alpha_{Ca^{2+}}$,[66] and on the basis of the size of the involved alkaline-earth metal ions, $r_{Ba^{2+}}$(1.61 Å) > $r_{Sr^{2+}}$(1.44 Å) > $r_{Ca^{2+}}$(1.34 Å), which will be of influence to the open space in the critical triangle. The quoted radii are taken from Shannon's compilation.[30] It is, however, likely that also other factors govern the migration barrier. Recent calculations on the formation and migration of oxygen vacancies in the series of $(La,Sr)(Co,Fe)O_{3-\delta}$ and $(Ba,Sr)(Co,Fe)O_{3-\delta}$ perovskites based on density functional theory suggest that it is the charge transfer from the migrating ion to the transition metal ion in the transition state and the local cation configuration in the critical triangle (containing, *e.g.*, 0, 1 or 2 Sr^{2+} ions) that would determine the energetic barrier.[67,68]

Conclusions

It is demonstrated in this study that LCF64 and LSF64 adopt slightly-distorted perovskite structures at room temperature to become ideal cubic (space group $Pm\bar{3}m$) at elevated temperatures. LBF64 adopts a cubic perovskite structure from room temperature up to 1000 °C. The different phase behaviour observed for the three compositions is suggested to be linked to the decreased tendency for tilting of the FeO_6 octahedra with increasing radius of the alkaline-earth-metal dopant ion.

Among the series LCF64, LSF64 and LBF64, the highest electrical conductivities in the temperature range 650–900 °C are found for LSF64. In air at 800 °C, the electrical conductivity of LSF64 is 191 S cm^{-1}, decreasing to a value of 114 S cm^{-1} at a pO_2 of 0.01 atm, and found over the entire pO_2 range roughly twice as high as those of LCF64 and LBF64. Unlike commonly suggested in literature, the temperature dependences of the electrical conductivities of the doped ferrite perovskite compositions could not be described by Holstein's small polaron theory. It is suggested that partial delocalization due to Fe 3d–O 2p hybridisation may change the nature of electronic conduction in these materials. Further research is required to elucidate this hypothesis.

A most important finding of our work is that the ionic conductivities of LCF64 and LSF64 as derived from data of electrical conductivity relaxation experiments in the temperature range 650–900 °C are high and fairly close to each other. The ionic conductivity of LCF64 at 650 °C is 1.2 × 10^{-3} S cm^{-1} while at 900 °C it is 44.6 × 10^{-3} S cm^{-1}, being a factor 3.6 and 1.44, respectively, lower than that for LBF64 showing the highest conductivity in this study. Noting that in general Ca-substituted materials are less vulnerable towards carbonation upon exposure to CO_2 as compared to substitution by Sr or Ba, this observation renders LCF64 a very promising cathode for use in IT-SOFCs.

Conflicts of interest

There are no conflicts to declare.

Acknowledgements

Financial support from the Dutch Technology Foundation (STW, now part of NWO; Project Nr. 15325) and the Chinese Scholarship Council (CSC 201406340102) are gratefully acknowledged.

References

1 A. Choudhury, H. Chandra and A. Arora, *Renewable Sustainable Energy Rev.*, 2013, **20**, 430–442.
2 S. B. Adler, *Chem. Rev.*, 2004, **104**, 4791–4843.
3 J. A. Lane, S. J. Benson, D. Waller and J. A. Kilner, *Solid State Ionics*, 1999, **121**, 201–208.
4 H. J. M. Bouwmeester, M. W. Den Otter and B. A. Boukamp, *J. Solid State Electrochem.*, 2004, **8**, 599–605.
5 H. Fan, Y. Zhang and M. Han, *J. Alloys Compd.*, 2017, **723**, 620–626.
6 Y. Niu, J. Sunarso, F. Liang, W. Zhou, Z. Zhu and Z. Shao, *J. Electrochem. Soc.*, 2011, **158**, 132–138.
7 T. Yu, X. Mao and G. Ma, *J. Alloys Compd.*, 2014, **608**, 30–34.
8 J. Hayd, L. Dieterle, U. Guntow, D. Gerthsen and E. Ivers-Tiffée, *J. Power Sources*, 2011, **196**, 7263–7270.
9 A. Jun, J. Kim, J. Shin and G. Kim, *ChemElectroChem*, 2016, **3**, 511–530.
10 C. Sun, R. Hui and J. Roller, *J. Solid State Electrochem.*, 2010, **14**, 1125–1144.
11 N. Mahato, A. Banerjee, A. Gupta, S. Omar and K. Balani, *Prog. Mater. Sci.*, 2015, **72**, 141–337.
12 R. J. D. Tilly, *Perovskites: Structure–Property Relationships*, John Wiley & Sons, Ltd, 2016.
13 J. Hayd, L. Dieterle, U. Guntow, D. Gerthsen and E. Ivers-Tiffée, *J. Power Sources*, 2011, **196**, 7263–7270.
14 Y. Teraoka, T. Nobunaga and N. Yamazoe, *Chem. Lett.*, 1988, 503–506.
15 C.-Y. Tsai, A. G. Dixon, Y. H. Ma, W. R. Moser and M. R. Pascucci, *J. Am. Ceram. Soc.*, 1998, **81**, 1437–1444.
16 J. W. Stevenson, *J. Electrochem. Soc.*, 2006, **143**, 2722–2729.
17 S. Li, W. Jin, P. Huang, N. Xu, J. Shi, Y. S. Lin, M. Z.-C. Hu and E. A. Payzant, *Ind. Eng. Chem. Res.*, 2002, **38**, 2963–2972.
18 F. H. Taylor, J. Buckeridge and C. R. A. Catlow, *Chem. Mater.*, 2017, **29**, 8147–8157.
19 F. Bidrawn, S. Lee, J. M. Vohs and R. J. Gorte, *J. Electrochem. Soc.*, 2008, **155**, B660–B665.
20 P. M. Price, E. Rabenberg, D. Thomsen, S. T. Misture and D. P. Butt, *J. Am. Ceram. Soc.*, 2014, **97**, 2241–2248.
21 L. Winnubst, S. A. Veldhuis, R. Ruhl, S. F. P. ten Donkelaar, H. J. M. Bouwmeester and A. Nijmeijer, *Ceram. Int.*, 2015, **41**, 13709–13715.
22 J. Rodríguez-carvajal, *Phys. B*, 1993, **15**, 49–55.
23 J. Mizusaki, M. Yoshihiro, S. Yamauchi and K. Fueki, *J. Solid State Chem.*, 1985, **58**, 257–266.
24 J. E. ten Elshof, M. H. R. Lankhorst and H. J. M. Bouwmeester, *J. Electrochem. Soc.*, 1997, **144**, 1060–1067.
25 M. W. den Otter, H. J. M. Bouwmeester, B. A. Boukamp and H. Verweij, *J. Electrochem. Soc.*, 2001, **148**, J1–J6.
26 M. H. Hung, M. V. M. Rao and D. S. Tsai, *Mater. Chem. Phys.*, 2007, **101**, 297–302.
27 J. B. Yang, W. B. Yelon, W. J. James, Z. Chu, M. Kornecki, Y. X. Xie, X. D. Zhou, H. U. Anderson, A. G. Joshi and S. K. Malik, *Phys. Rev. B: Condens. Matter Mater. Phys.*, 2002, **66**, 184415.
28 A. Ecija, K. Vidal, A. Larrañaga, A. Martínez-Amesti, L. Ortega-San-Martín and M. I. Arriortua, *Solid State Ionics*, 2011, **201**, 35–41.
29 A. Fossdal, M. Menon, I. Waernhus, K. Wiik, M.-A. Einarsrud and T. Grande, *J. Am. Ceram. Soc.*, 2010, **87**, 1952–1958.
30 R. D. Shannon, *Acta Crystallogr.*, 1976, **32**, 751–767.
31 V. M. Goldschmidt, *Naturwissenschaften*, 2005, **14**, 477–485.
32 J. B. Goodenough, *Rep. Prog. Phys.*, 2004, **67**, 1915–1993.
33 J. P. Attfield, *Int. J. Inorg. Mater.*, 2001, **3**, 1147–1152.
34 A. M. Glazer, *Acta Crystallogr., Sect. B: Struct. Crystallogr. Cryst. Chem.*, 1972, **28**, 3384–3392.
35 C. J. Howard and H. T. Stokes, *Acta Crystallogr., Sect. B: Struct. Sci.*, 1998, **54**, 782–789.
36 C. J. Howard and H. T. Stokes, *Acta Crystallogr., Sect. A: Found. Crystallogr.*, 2005, **61**, 93–111.
37 M. Kuhn, S. Hashimoto, K. Sato, K. Yashiro and J. Mizusaki, *Solid State Ionics*, 2011, **195**, 7–15.
38 V. V. Kharton, A. V. Kovalevsky, M. V. Patrakeev, E. V. Tsipis, A. P. Viskup, V. A. Kolotygin, A. A. Yaremchenko, A. L. Shaula, E. V. Kiselev and J. C. Waerenborgh, *Chem. Mater.*, 2008, **20**, 6457–6467.
39 M. Søgaard, P. Vang Hendriksen and M. Mogensen, *J. Solid State Chem.*, 2007, **180**, 1489–1503.
40 W. H. Jung and E. Iguchi, *J. Phys.: Condens. Matter*, 1995, **7**, 1215–1227.
41 A. Benali, A. Souissi, M. Bejar, E. Dhahri, M. F. P. Graça and M. A. Valente, *Chem. Phys. Lett.*, 2015, **637**, 7–12.
42 H. C. Wang, C. L. Wang, J. L. Zhang, W. B. Su, J. Liu, M. L. Zhao, N. Yin, Y. G. Lv and L. M. Mei, *Curr. Appl. Phys.*, 2010, **10**, 866–870.
43 J. Mizusaki, T. Sasamoto, W. R. Cannon and H. K. Bowen, *J. Am. Ceram. Soc.*, 1983, **66**, 247–252.
44 F. A. Kröger and H. J. Vink, *Solid State Phys.*, 1956, **3**, 307–435.
45 T. Holstein, *Ann. Phys.*, 1959, **8**, 343–389.
46 D. Emin and T. Holstein, *Ann. Phys.*, 1969, **53**, 439–520.
47 L. Friedman and T. Holstein, *Ann. Phys.*, 1963, **21**, 494–549.
48 K. J. Yoon, P. a. Zink, S. Gopalan, U. B. Pal and L. R. Pederson, *J. Electrochem. Soc.*, 2009, **156**, B795–B800.
49 M. V. Patrakeev, I. A. Leonidov, V. L. Kozhevnikov and K. R. Poeppelmeier, *J. Solid State Chem.*, 2005, **178**, 921–927.
50 L. Tai, M. Nasrallah, H. Anderson, D. Sparlin and S. Sehlin, *Solid State Ionics*, 1995, **76**, 259–271.
51 C. Zener, *Phys. Rev.*, 1951, **82**, 403–405.
52 M. Abbate, F. M. F. de Groot, J. C. Fuggle, A. Fujimori, O. Strebel, F. Lopez, M. Domke, G. Kaindl, G. A. Sawatzky, M. Takano, Y. Takeda, H. Eisaki and S. Uchida, *Phys. Rev. B: Condens. Matter Mater. Phys.*, 1992, **46**, 4511–4519.
53 A. M. Ritzmann, A. B. Muñoz-García, M. Pavone, J. A. Keith and E. A. Carter, *Chem. Mater.*, 2013, **25**, 3011–3019.
54 J. Suntivich, W. T. Hong, Y. L. Lee, J. M. Rondinelli, W. Yang, J. B. Goodenough, B. Dabrowski, J. W. Freeland and Y. Shao-Horn, *J. Phys. Chem. C*, 2014, **118**, 1856–1863.
55 R. Pushpa, D. Daniel and D. P. Butt, *Solid State Ionics*, 2013, **249–250**, 184–190.
56 D. G. Daniel, *The Electronic and Thermodynamic Properties of Ca Doped LaFeO3 – A First Principles Study Using Density Functional Theory*, 2014.

57 L. Wang, Y. Du, P. V. Sushko, M. E. Bowden, K. A. Stoerzinger, S. M. Heald, M. D. Scafetta, T. C. Kaspar and S. A. Chambers, *Phys. Rev. Mater.*, 2019, **3**, 025401.
58 C. L. Chang, G. Chern, M. F. Tai, Y. W. Su, C. L. Dong, S. Y. Liu, C. S. Hwang and P. K. Tseng, *Jpn. J. Appl. Phys.*, 1999, **38**, 108–110.
59 H. Wadati, A. Chikamatsu, M. Takizawa, R. Hashimoto, H. Kumigashira, T. Yoshida, T. Mizokawa, A. Fujimori, M. Oshima, M. Lippmaa, M. Kawasaki and H. Koinuma, *Phys. Rev. B: Condens. Matter Mater. Phys.*, 2006, **74**, 115114.
60 T. Ishigaki, S. Yamauchi, K. Kishio, J. Mizusaki and K. Fueki, *J. Solid State Chem.*, 1988, **73**, 179–187.
61 J. Yoo, A. Verma, S. Wang and A. J. Jacobson, *J. Electrochem. Soc.*, 2005, **152**, A497–A505.
62 H. J. M. Bouwmeester and A. J. Burggraaf, in *The CRC Handbook of Solid State Electrochemistry*, ed. P. J. Gellings and H. J. M. Bouwmeester, CRC, New York, 1997, p. 481.
63 C. Berger, E. Bucher, A. Windischbacher, A. D. Boese and W. Sitte, *J. Solid State Chem.*, 2018, **259**, 57–66.
64 C. Berger, E. Bucher and W. Sitte, *Solid State Ionics*, 2017, **299**, 46–54.
65 J. A. Kilner and R. J. Brook, *Solid State Ionics*, 1982, **6**, 237–252.
66 J. Mitroy, M. S. Safronova and C. W. Clark, *J. Phys. B: At., Mol. Opt. Phys.*, 2010, **43**, 1–44.
67 Y. A. Mastrikov, R. Merkle, E. A. Kotomin, M. M. Kuklja and J. Maier, *Phys. Chem. Chem. Phys.*, 2013, **15**, 911–918.
68 C. Wessel, M. W. Lumey and R. Dronskowski, *J. Membr. Sci.*, 2011, **366**, 92–96.